Journal Pre-proof

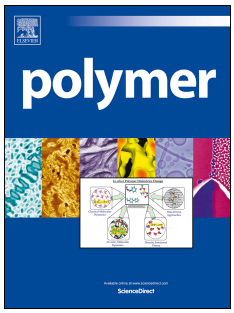

High-performance nanoporous aramid films reinforced with functionalized carbon nanocharges using ionic liquids

Miriam Trigo-López, S. Vallejos, José A. Reglero Ruiz, Alejandra García-Gómez, María Seara-Martínez, Félix C. García, José M. García

PII: S0032-3861(20)30460-2

DOI: https://doi.org/10.1016/j.polymer.2020.122629

Reference: JPOL 122629

To appear in: *Polymer*

Received Date: 13 March 2020

Revised Date: 5 May 2020

Accepted Date: 17 May 2020

Please cite this article as: Trigo-López M, Vallejos S, Reglero Ruiz JoséA, García-Gómez A, Seara-Martínez Marí, García FéC, García JoséM, High-performance nanoporous aramid films reinforced with functionalized carbon nanocharges using ionic liquids, *Polymer* (2020), doi: https://doi.org/10.1016/j.polymer.2020.122629.

Miriam Trigo-López: Synthesis of the polyamide model, Fabrication of the aramid films **S. Vallejos:** Functionalization of the nanocharges, Fabrication of the aramid films **José A. Reglero Ruiz:** Characterization of materials, Writing of the manuscript **Alejandra García-Gómez:** Synthesis of the graphene **María Seara-Martínez:** Synthesis of the graphene **Félix C. García:** Supervision, Writing and Reviewing **José M. García:** Supervision, Writing and Reviewing.

High-performance nanoporous aramid films reinforced with functionalized carbon nanocharges using ionic liquids

Miriam Trigo-López[1], S. Vallejos[1], José A. Reglero Ruiz*[,1], Alejandra García-Gómez[2], María Seara-Martínez[2], Félix C. García[1] and José M. García*[,1].

[1] Departamento de Química, Facultad de Ciencias, Universidad de Burgos, Plaza de Misael Bañuelos s/n, 09001 Burgos, Spain. Tel: +34 947 258 085.

[2] Gnanomat S.L. Campus Cantoblanco, Spain Madrid Science Park, Faraday Street, 7, 28049 Madrid, Spain. Tel: +34 910 800 806.

*Corresponding authors Emails: jareglero@ubu.es ; jmiguel@ubu.es

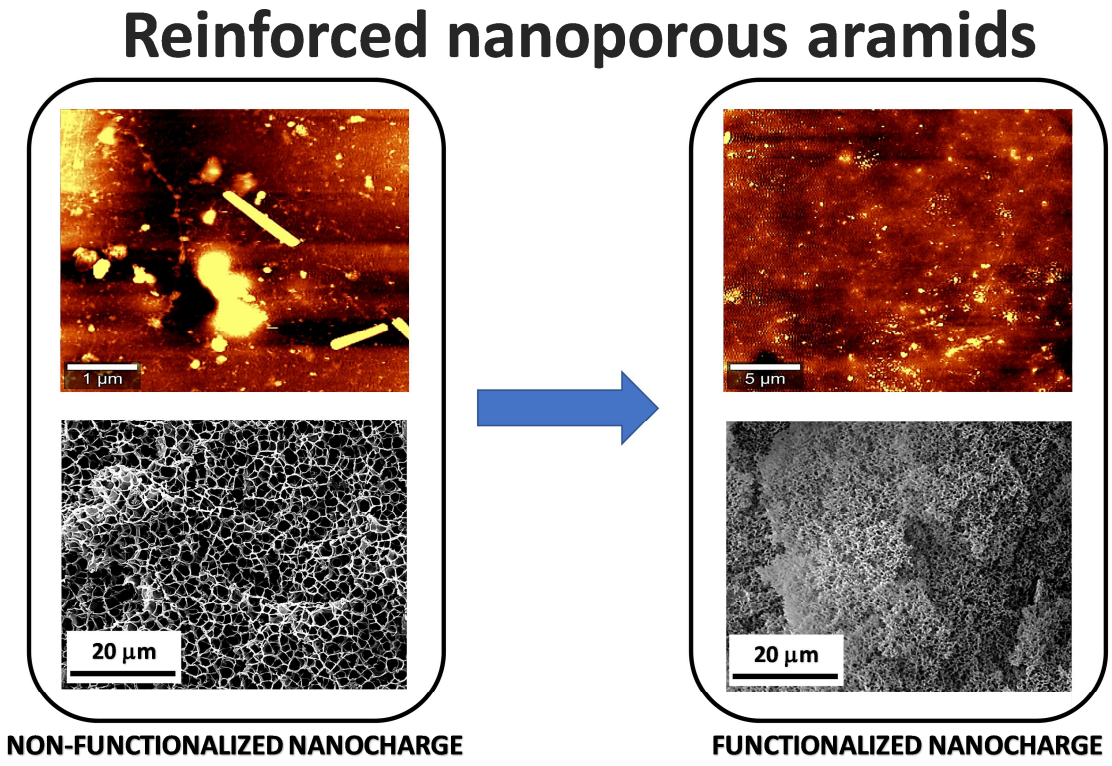

High-performance nanoporous aramid films reinforced with functionalized carbon nanocharges using ionic liquids

Miriam Trigo-López[1], S. Vallejos[1], José A. Reglero Ruiz*[,1], Alejandra García-Gómez[2], María Seara-Martínez[2], Félix C. García[1] and José M. García*[,1].

[1] Departamento de Química, Facultad de Ciencias, Universidad de Burgos, Plaza de Misael Bañuelos s/n, 09001 Burgos, Spain. Tel: +34 947 258 085.

[2] Gnanomat S.L. Campus Cantoblanco, Madrid Science Park, Faraday Street, 7, 28049 Madrid, Spain. Tel: +34 910 800 806.

*Corresponding author E-mails: jareglero@ubu.es (José A. Reglero Ruiz); jmiguel@ubu.es (José M. García)

Abstract

We prepare low density nanoporous aramid films reinforced with carbon-based nanocharges (graphene, carbon nanofibers and carbon nanotubes), using ionic liquids to generate and control the porous structure, reaching a density reduction of about 4 times and pore sizes down to 240 nm. Because of the low dispersion ability of the nanocharges in the aramid matrix, we carried out a novel functionalization process in which nanocharges were chemically modified by anchoring a polyamide model to their surface. Then, we tested the different behavior of the aramid films reinforced with neat and functionalized nanocharges, observing that functionalization led to better nanocharges dispersion, reduction of pore size from the micrometer to the nanometer range and the improvement of the mechanical behavior, resulting in higher relative Young's moduli values (around 60% higher in porous aramids reinforced with functionalized nanocharges).

Keywords: nanoporous aramid; carbon nanocharge; ionic liquid

1. Introduction

Aromatic polyamides or aramids are high-performance materials because of their outstanding mechanical strength and thermal resistance. Aramids are usually spun into fibers or dense membranes and they are employed for advanced fabrics in applications in which high thermal and mechanical stability is required [1,2].

Concerning membrane technology, the improvement of aramid membranes is carried out twofold. First, by reinforcing them with nanofillers (carbon-based nanocharges mainly); and second, by obtaining a controlled micro and nanoporosity in the membrane to reduce their density while maintaining their outstanding mechanical and thermal performance.

To improve the mechanical properties of composite materials with nanofillers, a good dispersion of the nanofillers together with an effective interfacial interaction with the matrix and good load transfer are needed [3]. However, nanocharges aggregate in the form of clusters, and chemical modification of the graphitic surfaces has showed to provide a significant increase in the modulus of the composites compared to the matrix, and so contributing to a better dispersion and an efficient thermodynamic wetting of nanocharges with the polymer matrices [4]. For that purpose, different strategies have been followed, such as the direct functionalization (carbene and nitrene addition, halogenation, etc.) [5,6], or the defect functionalization through oxidative processes [7,8]. To incorporate carbon nanofillers in aramids, different approaches such as a solution casting method of unmodified carbon nanotubes or graphene [9,10], the diffusion of carbon nanotubes in solvent swelled Kevlar fibers [11,12]. or the compatibilization the aramids with polydopamine to increase the interactions between the matrix and the nanofiller [13] were followed. Other strategies include the hydrolyzation of the aramid fibers to get acid and amine groups [14] and mix them with acid chloride functionalized nanofillers [15,16].

The second line to improve the properties of aramid membranes is focused on the generation of controlled nano porous structure, to reduce their weight without lowering their thermal and mechanical characteristics. Traditionally, Supercritical CO_2 ($ScCO_2$) has been used to develop this porous structure [17]. However, it is not adequate for aramids because of their high thermal stability, high crystallinity degree and also their low CO_2 affinity. Recently, our research group published two innovative research works in which nanoporous membranes based on laboratory synthetized aramids were successfully obtained in a simple and easy way using ILs [18,19]. These two works were based in obtaining porous materials based on synthetized aramids, using two different routes: through the addition of ILs, which where after removed in distilled

water to get the porous structure, or by using these ILs as CO_2 capture promoters to foam aramids in a single-step $ScCO_2$ batch process. In both preliminary papers, synthetized (thus, no commercial) aramids were used, and no reinforcements (in terms of carbon-based nanofillers) were used.

This work intends to go one step further in the improvement of the properties of aramids, using in this case commercial poly(*m*-phenylene isophtalamide, PA), and aiming to get micro- and nano porous aramid membranes reinforced with different previously-functionalized carbon nanofillers (graphene, carbon nanotubes and carbon nanofibers).

To fulfill this purpose, two different steps were taken in this work. First, the functionalization of the carbon nanofillers with an aramid-like moiety (model polyamide) to induce repulsion between the particles and to enhance their interaction with the aramid matrix, thus improving the dispersion. And second, preparing aramids reinforced with modified carbon nanofillers having a controlled micro and nano porosity by using ionic liquids (ILs).

2. Materials

All materials and solvents were commercially available and used as received, unless otherwise indicated. 4-nitrobenzoyl chloride (98% , Sigma-Aldrich), 5-aminoisophthalic acid (98%, Merk), acetic acid (100%, Merk), palladium on carbon 10% weight (Pd/C, Sigma-Aldrich), methanol (99.8%, Sigma-Aldrich), ethanol (99.9%, VWR-Chemicals), dimethyl sulfoxide (DMSO, 99%, Prolabo), hydrochloric acid (37%, VWR-Chemicals), sodium nitrite (99%, Panreac), sodium azide (99%, Alfa-Aesar), thionyl chloride (99%, Merk), heptane (99.9%, VWR-Prolabo), aniline (99%, Sigma-Aldrich) and deuterated dimethyl sulfoxide (DMSO-d_6) (99.80D, VWR-Chemicals).

The ionic liquid (IL) used was 1-ethyl-3-methylimidazolium bromide (≥ 97%, Sigma-Aldrich, used as received), and *N,N*-dimethylacetamide (DMAc, Aldrich, > 99%, used as received).

Commercial *meta*-aramid fiber ARAWIN® (PA) (Nonwoven regular staple fiber of average length 6.4 mm), was supplied by Toray Advanced Materials Inc. (Korea), and used as received.

Three different carbon-based nanocharges used, all of them received in powder form. The graphene nanoplatelet powder used in this study was provided by 2-DTech Ltd., part of Versarien plc., UK, produced using a mechanochemical process based on patented procedures [20]. This graphene nanoplatelet was modified by adding 15% wt.

of carbon black to increase its electrical conductivity (GN/CB), using a ball milling equipment model IKA ULTRA-TURRAX Tube Drive, during 5 min at 6000 rpm. Carbon nanofibers (NF) graphitized (iron-free) composed of conical platelets (D x L ≈ 100 nm x 20-200 μm) were supplied by Sigma Aldrich. Finally, single-walled carbon nanotubes (NT) were supplied by Dropsens (80 % purity, D x L ≈ 20 nm x 5-10 μm).

Dense aramid materials were prepared as follows: First, the aramid fiber and the IL were dissolved in DMAc. A mixture of a 75/25 proportion of IL respect to MPIA fiber was added to the aramid fiber solution. In order to improve the solubility of aramid fiber in DMAc, a fixed proportion of LiCl (2 % wt. respect to the volume of DMAc) was added to the solution, which is stirred during 1 hour at RT. After this first stage, the solution is filtered, and 1 % wt. of the nanocharges (respect to the aramid fiber weight) was added. The solution is taken under magnetic stirring for 8 hours at RT, followed by a sonication process in an ultrasonic bath for 3 hours, to achieve complete homogenization. For the NT, and due to their poor functionalization, the solution was stirred up to 72 h until full homogenization. Then, the solution is poured into a glass plate of 20 x 20 cm and placed inside an oven at 60 ºC during at least 24 h, until the complete evaporation of the solvent. Finally, films were washed in distilled water at 80 ºC during 4 hours to remove any traces of solvent.

3. Characterization methods

^{1}H and ^{13}C NMR spectra were recorded with a Varian Inova 300 spectrometer operating at 300 and 75.5 MHz, respectively, with deuterated dimethyl sulfoxide (DMSO-d_6) as solvent. Infrared spectra (FTIR) were recorded with a FT/IR-4200 FTIR Jasco Spectrometer with an ATR-PRO410-S single reflection accessory.

Porous morphology of the aramid films after IL removal was deeply analyzed in the cross section and surface of the samples from SEM and AFM images, respectively.

SEM micrographs were taken using a Scanning Electronic Microscope Model FEI ESEM Quanta 600, provided by the CENIEH (Centro Nacional de Investigación sobre la Evolución Humana, Burgos). Films were frozen in liquid nitrogen, fractured and gold coated in vacuum to assure the electrical conductivity of the films. Cellular structural characterization determining the average bubble radius $\bar{R}$ and average cell density from SEM images was measured using ImageJ® software and comprised counting the number of bubbles in each image n_i and its radius R_i [21]. ~~The average radius was calculated using Equation 1.~~

~~$$\bar{R} = \frac{\sum_{i=1}^{N} n_i R_i}{\sum_{i=1}^{N} n_i}$$~~

~~(1)~~

~~where *N* represents the bubble count.~~ Three different SEM images were analyzed from each material, and the data was averaged. The estimation of the cell density N_c was calculated using the Kumar's approximation, as shown in Equation 1.

$$N_c = \left(\frac{n}{A}\right)^{3/2}$$

(1)

where *n* is the number of cells in the image and *A* is the area of the image. The description of the calculation method can be found in our previous work [22].

Atomic Force Microscopy (AFM) images were taken using a confocal AFM-RAMAN model Alpha300R – Alpha300A from WITec, using a AFM tip of 42 N/m. Images were taken at RT. Transmission Electron Microscopy (TEM) images were carried out in a TEM equipment, model JEOL JEM 1011. Samples were cut at RT in slides of 70 nm thickness using a microtome model Powertome PC (RCM Products). This equipment was provided by the Parque Científico of the University of Valladolid.

Density was determined from the dimensions and weight of the samples. In solid samples, thickness was determined directly using a digital micrometer. In porous samples, thickness was measured from SEM images.

Thermal properties of the aramid films were determined through DSC and TGA experiments to test the efficiency of the IL removal process by analyzing the thermal data of films before and after the immersion in distilled water, and the influence of the addition of the nanocharges in the glass transition temperature and in the thermal stability of the aramid films.

Differential Scanning Calorimetry (DSC) tests were performed in a DSC Q200 TA Instruments to evaluate the thermal transitions of the materials. First, after 5 min of stabilization at 30 ºC, films were heated to 350 ºC at 15 ºC/min. Then, the samples were stabilized for 5 min at 350 ºC and cooled down to -80 ºC to erase the thermal history. Then, a second heating ramp up to 350 ºC was carried out at 15 ºC/min. The samples were again cooled down to -80 ºC at 15 ºC/min, and finally, samples were heated up to RT at 15 ºC/min. All tests were performed under N_2 atmosphere (flow rate 50 ml/min), with a mass sample of approximately 15 mg. The thermogravimetric analysis data were recorded on a TA Instrument Q50 TGA analyzer. TGA tests were

performed under O_2 (synthetic air) or N_2 atmosphere using the next procedure: first, samples were heated from RT to 100 °C at 10 °C/min, and then kept during 10 min to eliminate the moisture content. Then, samples were heated in the selected atmosphere (O_2 or N_2) up to 800 ºC at 10 ºC/min.

An elemental organic microanalyzer model Thermo Scientific Flash 2000 was used to measure the quantity of carbon, hydrogen, nitrogen and Sulphur (CHNS test). Three replicates of each sample were performed, using approximately 1 mg in each test.

A set of tensile tests was carried out covering all the fabricated films, both dense and porous, to test the combined effect of the nanocharges and their functionalization together with the generation of the porous structure in the mechanical properties. To determine the mechanical properties, 5 x 40 mm strips were cut from the films, and tensile tests were performed on a SHIMADZU EZ Test Compact Table-Top Universal Tester. Mechanical clamps were used, and an extension rate of 5 mm/min was applied using a gauge length of 9.44 mm. At least 5 samples were tested for each film, and the data were then averaged. The Young's modulus and stress-strain values at break were obtained.

4. Results and discussion

4.1 Functionalization of nanocharges

The surface of three different nanocharges (carbon nanofibers, carbon nanotubes and graphene) was functionalized with a model polyamide. The model polyamide (**5**) was prepared following common organic synthetic procedures, according to **Figure 1**. The synthesis and characterization of all the intermediates and the model polyamide is described in the **Section 1** of the **Electronic Supplementary Information** (**ESI**).

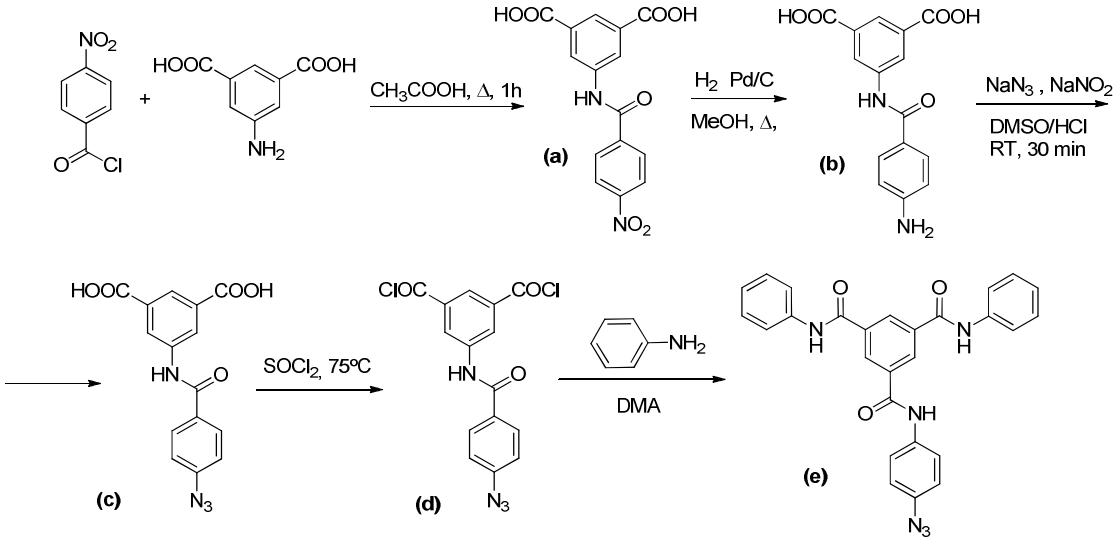

Figure 1. Synthesis of model polyamide (**5**)

The nanocharges are functionalized suspended in a solution of DMA at 150 ºC containing the model polyamide according to the procedure described in **Section 2** of the **ESI**. The functionalization is based on the nitrene chemistry, where a cycloaddition [2+1] of nitrenes to the double bonds of the nanofiller occurs, using model polyamides containing an azide group[23].

Elemental analysis CHNS of the neat and functionalized nanocharges was performed to determine the nitrogen quantity derived from the anchored model polyamide, to study comparatively the efficiency of the functionalization process. We detected that the functionalization of the NF was much more effective (up to 2 times) than the functionalization of the NT (10.4 %wt. of nitrogen in the case of NF vs 4.8 %wt. of nitrogen in NT). The functionalization of GN /CB resulted in only 2.9 %wt. of nitrogen, probably because of the high content of black carbon (15 %wt. respect to graphene), which cannot be functionalized. The effectiveness of the functionalization of the nanocharges with the polyamide model can be also carried out through the comparison of the thermogravimetric curves of neat and functionalized nanocharges, as it is shown in **Figure S7** in the **ESI,** in which the mass loss associated to the polyamide model employed in the functionalization process of each nanocharge is clearly detected. It is important to notice that a direct correlation between the quantity of nitrogen detected in the CHNS analysis and the percentage of mass loss observed in the TGA curves cannot be stablished, since it also depends on the deterioration of the carbon nanocharge surface because of the functionalization procedure. It is observed that GN/CB presents the higher and faster percentage of mass loss, maybe due to the decomposition of the carbon black, followed by NT and NF (**Figures S7b**, **S7c** and **S7d** in the **ESI**). We additionally include in **Figure S7a** the thermogram of the synthetized polyamide model, in which the decomposition of the azide groups is observed around 200 ºC.

To simplify the notation in the manuscript, from this point “neat” nanocharges will be further simply denoted as nanocharges, and on the other hand, when “functionalized” are employed, this term will be specifically mentioned. The term “pure” will be exclusively used for non-reinforced aramid films.

4.2. Aramid films

To test the influence of the modification of the nanocharges in the aramid properties and in the porosity, 12 different dense films were prepared, with and without ionic

liquids, and with or without functionalized nanocharges, according to **Table S1.** Dense aramid films were prepared following the procedure described in Materials section. Two additional films were prepared from pure PA (with and without ionic liquids). The thicknesses of all the dense films produced varied between 210 and 230 μm, and the density of the films prepared is described in **Table S1** of the **ESI**.

For the generation of the porous structure, dense films containing IL were washed for 5 hours in distilled water at 80 °C, replacing it three times to remove the IL completely. The black color of the film related to the presence of the nanocharges turns grey when the porous structure is generated (See **Figure S8** of the **ESI**), which was also observed in our previous work [24]. **Table 1** presents the density values of porous films (ρ), the relative density in relation with the density of dense films (ρ_r) and the nomenclature employed to name the porous films obtained. A density reduction between 3 and 4 times respect to dense film is observed, with a minimum value of 0.38 g/cm^3 in the case of (PA+NT+IL)^f-R and a maximum value of 0.48 g/cm^3 for the (PA+NF+IL)^f-R. Measured density of the dense aramids was around 1.38 g/cm^3. Although the proportion of IL is the same in all the porous films, density values are not exclusively related to the IL quantity, pointing out an influence of the nanocharge employed in the weight reduction. For example, the use of NF renders higher density values (thus lower weight reduction) than films reinforced with NT. Moreover, the functionalization process also has an influence in the density of porous films, showing slightly higher density values using functionalized nanocharges (**Table 1**).

Table 1 – Nomenclature and density of the porous aramid films produced after IL removal. "-R" indicates the removal of the IL.

Nomenclature	ρ (g/cm^3)	ρ_r
(PA+IL)-R	0.47	0.39
(PA+NF+IL)-R	0.40	0.34
(PA+NT+IL)-R	0.29	0.23
(PA+GN/CB+IL)-R	0.41	0.33
(PA+NF+IL)^f-R	0.48	0.38
(PA+NT+IL)^f-R	0.38	0.30
(PA+GN/CB+IL)^f-R	0.42	0.34

4.3 Dispersion of nanocharges

~~One of the main objectives of the research work was related to the improvement of the dispersion of the nanocharges because of the functionalization process and its influence in the porous structure, and in the thermal and mechanical properties of~~

~~aramid films. The analysis of the dispersion can be carried out from different perspectives, such as through the direct visualization of the nanocharges distribution in the aramid matrix, through AFM surface images, through TEM observations, or from the tensile tests that evidence the efficiency of the mechanical load transfer between the nonocharge and the matrix.~~

The effectiveness of the functionalization process was related to the improvement of the dispersion of the nanocharges. Visual evaluation of the dispersion is presented in **Figure 2,** which shows the visual appearance of the aramid films reinforced with the nanocharges (NF, NT and GN/CB). The photographs of the aramid films were taken with a homemade closed retro-illumination device prepared with a Prusa i3 Steel 3D printer using the backlight system of a cheap commercial tablet. [25]

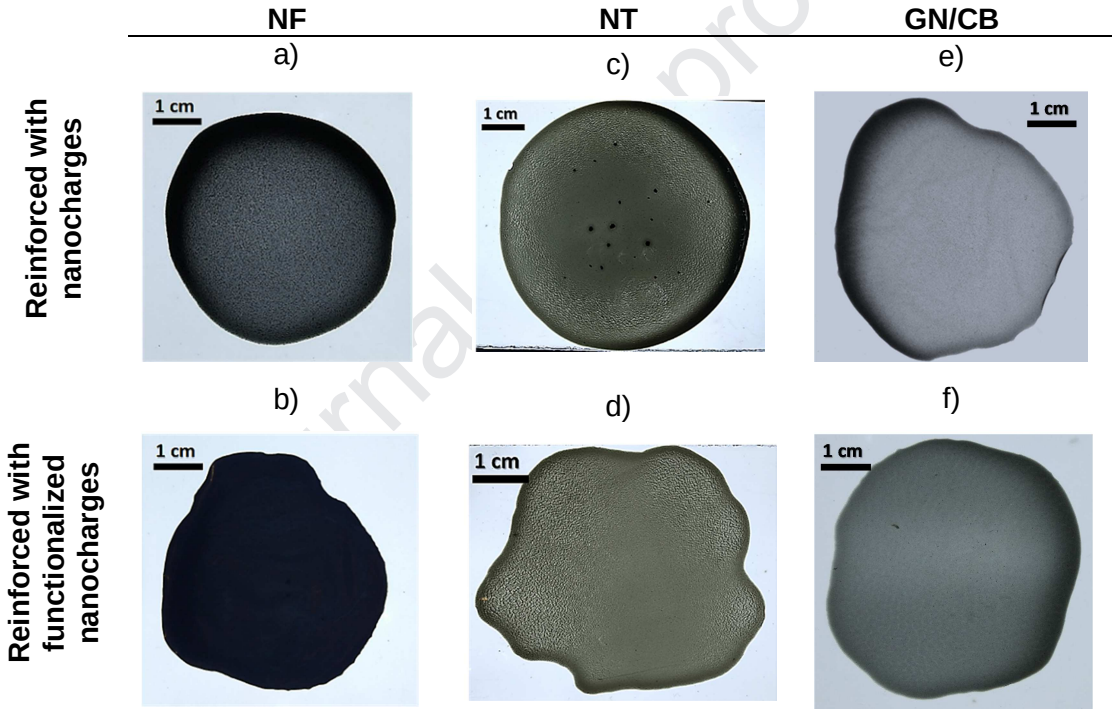

Figure 2 – Photographs of the dense aramid films. a) (PA+NF); b) (PA+NF)^{f}; c) (PA+NT); d) (PA+NT)^{f}; e) (PA+GN/CB); f) (PA+GN/CB)^{f}

The dispersion is greatly improved in the case of the functionalization of the NF, as it can be seen in **Figures 2a** (NF) and **2b** (functionalized NF). Non-dispersed NF are observed in the center of the film (black dots) in **2a**. This lack of dispersion leads to inhomogeneous materials, thus limiting drastically their final properties. The functionalization of the NF results in a very homogeneous aramid film, with a homogeneous opacity observed in all the surface, confirming the excellent dispersion grade of the functionalized nanocharges as a consequence of the high functionalization

evidenced by the CHNS analysis. ~~This remarkable improvement in the dispersion of nanocharges can be related to the high functionalization of the nanocharges, evidenced by the high content of nitrogen detected in the CHNS analysis (10.4%wt. of N)~~. In the case of NT and GN/CB, the improvement of the dispersion when using functionalized nanocharges is not so pronounced. The functionalization of the NT seems to be slightly effective, and the agglomerated nuclei observed in aramid films with NT (**Figure 2c**) are not present when functionalized NT are employed (**Figure 2d**). The functionalization of GN/CB also leads to a better dispersion in the aramid matrix, as it is shown in **Figures 2e** (GN/CB) and **2f** (functionalized GN/CB). Here, although the nitrogen percentage detected is the lowest ~~(2.89%wt.)~~, the improvement in the dispersion could be because of the positive effect of black carbon.

AFM surface images were collected to analyze the dispersion and functionalization effect of the nanocharges, allowing to detect individual nanocharges standing out of the surface of the matrix (**Figure 3**).

For NF dispersed in the aramid (**Figure 3a**), isolated NF lying in the aramid surface can be observed, together with a typical agglomeration in the center where NF reach heights of around 100 nm above the aramid matrix surface (yellow regions show regions higher in distance to the surface with respect to the aramid matrix). On the contrary, the functionalization procedure results in a better dispersion (**Figure 3b**). The functionalization also prevents the appearance of isolated NF in the surface, embedding the nanocharges in the polymer matrix.

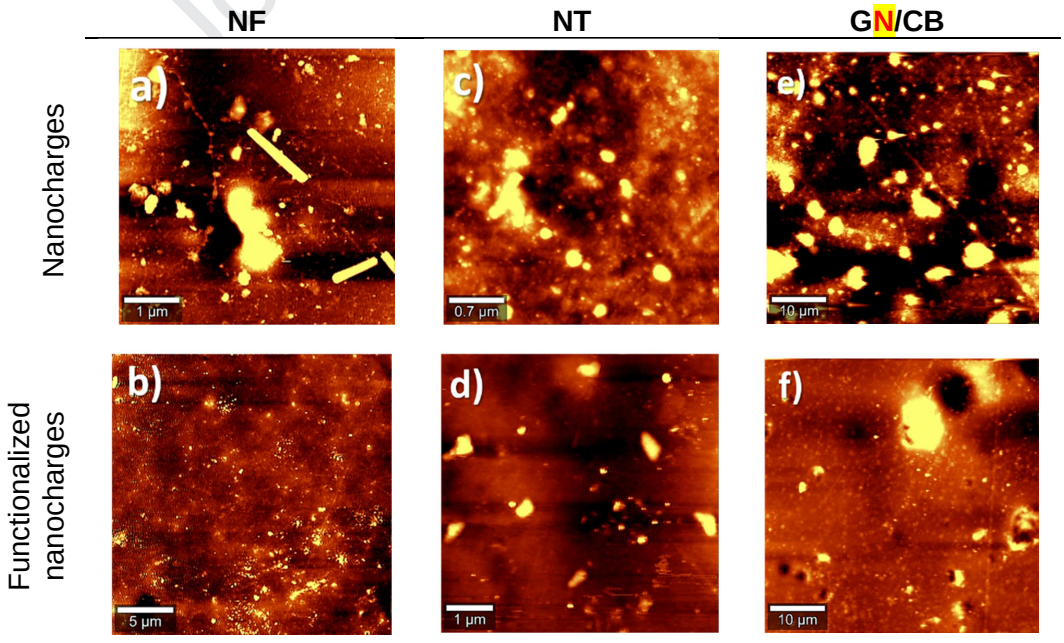

Figure 3. AFM surface images of the dense aramid films. a) (PA+NF); b) (PA+NF)^{f}; c) (PA+NT); d) (PA+NT)^{f}; e) (PA+GN/CB); f) (PA+GN/CB)^{f}

The same phenomenon is observed for NT and GN/CB: the reinforcement of aramids with functionalized NT or GN/CB (**Figures 3d** and **3f**) lead to more homogeneous distributions in the aramid compared to NT and GN/CB (**Figures 3c** and **3e**), where agglomerations are evidenced. As observed in the case of NF, it seems that the functionalization process reduced the presence of nanocharges in the surface of the aramid, embedding again the nanocharges inside the aramid matrix. Also, in **Figure 3e**, carbon black can be differentiated from graphene (carbon black diameter varies between 5 and 20 μm, whereas graphene nanoplatelets size is below 1 μm), and when functionalized GN/CB is used (**Figure 3f**), it seems that individual carbon black particles are dispersed inside the polymer matrix, and only isolated particles are observed in the surface.

TEM images were collected to investigate in more detail the dispersion of the nanocharges and the effectiveness of the functionalization process. We observed, after preparing and cutting of the samples in the microtome, that although the thickness was reduced down to 70 nm, films presented a high opacity due to the presence of the nanocharges, impairing the transmission of the electrons through the sample and limiting the obtention of the images. For this reason, it was not possible to get images of the dispersion of the nanocharges in the polymer matrix. However, we include here some TEM pictures of the edges of the samples (**Figures 4a**) where functionalized NF are not agglomerated, but embedded in the aramid matrix. ~~In **Figure 4b**,~~ Also, the polymer matrix between the functionalized NF is clearly evidenced.

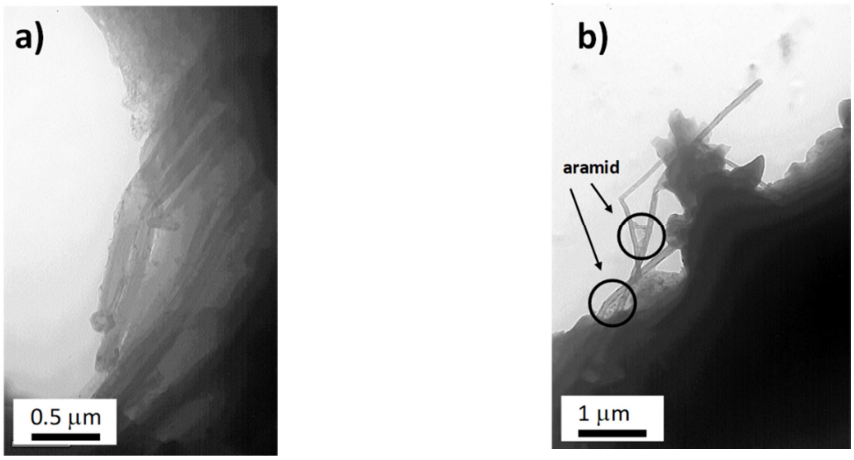

Figure 4. TEM images of the functionalized NF embedded in the aramid films.

4.4 Porous morphology

A very homogeneous porous structure is revealed after the IL removal in pure aramid films, with pore sizes below 1 μm and high cell density, as evidenced in **Figure 5a**. The porous structure extended along the whole thickness of the film, and no typical solid outer skin derived from the classical $ScCO_2$ process was observed [26].

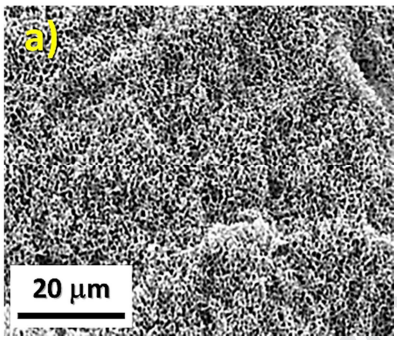

(PA+IL)-R

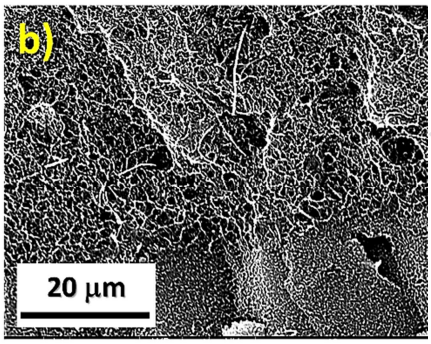

(PA+NF+IL)-R

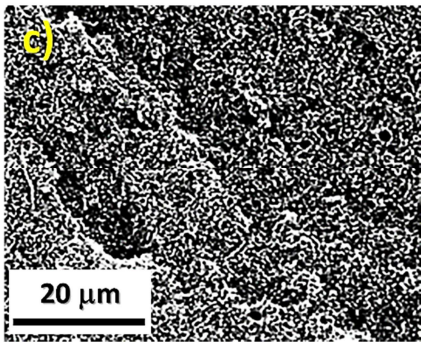

(PA+NF+IL)^{t}-R

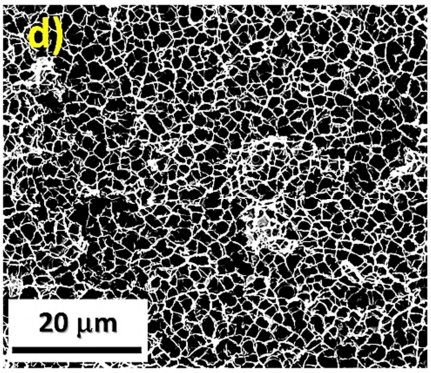

(PA+NT+IL)-R

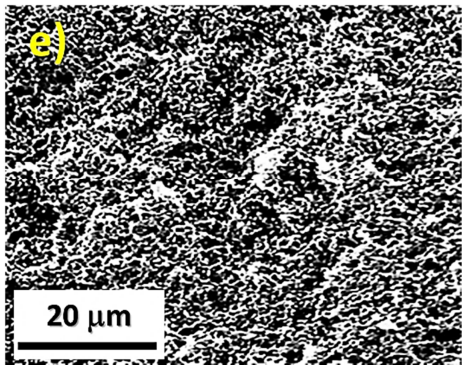

(PA+NT+IL)^{f}-R

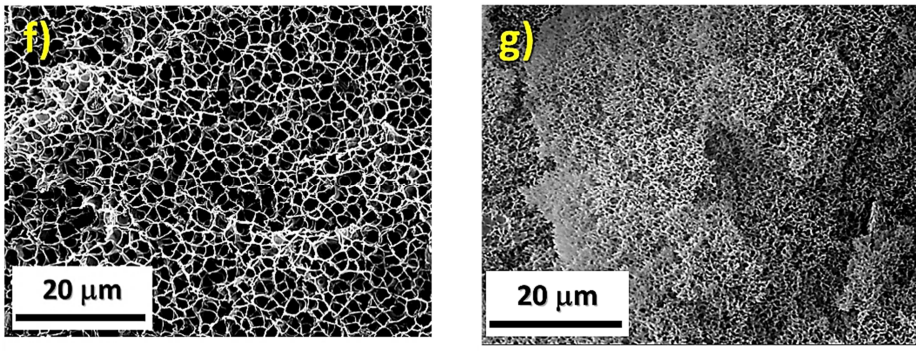

(PA+GN/CB+IL)-R (PA+GN/CB+IL)^{f}-R

Figure 5. SEM micrographs of the cross section of a) (PA+IL)-R, b) (PA+NF+IL)-R, c) (PA+NF+IL)^{f}-R, d) (PA+NT+IL)-R, e) (PA+NT+IL)^{f}-R, f) (PA+GN/CB+IL)-R, g) (PA+GN/CB+IL)^{f}-R.

The effect of the functionalization of nanocharges is also analyzed in the comparative cross-section SEM images of porous aramid films reinforced with nanocharges. A clear inhomogeneous structure is observed for the aramid film reinforced with NF, where NF are concentrated in half of the width (**Figure 5b**) coinciding with a porous structure. However, the film presents a solid region in which no porous structure is evidenced, so a relationship between the deficient dispersion of the NF and the inhomogeneity of the porous structure can occur. ~~Considering that the porous structure is generated by the IL removal process, it seems to be a direct relation between the NF and IL dispersion in the initial DMAc solution, resulting in a very inhomogeneous structure~~. On the contrary, the functionalization of the NF leads to a very different porous structure (**Figure 5c**), thus obtaining a homogeneous porous morphology with small pore sizes and high cell densities. To conclude, both SEM images also shows isolated fibers along the porous structure~~, which are embedded in the polymer matrix, as also observed in the AFM images~~.

The effect of the functionalization in the porous aramid films reinforced with NT is also remarkable (**Figure 5d** and **e**). A microporous structure of pore size around several µm is obtained for the aramid reinforced with non-functionalized NT (**d**), very different from the morphology observed in the case of pure aramid. The addition of NT hinders the formation of a fine nanoporous structure, while using functionalized NT (**e**) reduces drastically the pore size below 1 µm, then reaching the nanoporous range, in a very fine a homogeneous structure. In this case, isolated NT were not observed, but it is possible that due to their low size they could be along the cell walls in the porous structure.

The porous structure obtained for aramids reinforced with GN/CB is very similar to the one observed for the NF (**Figure 5f**). In this case, the use of GN/CB does not improve the morphology of pure aramid film, and only pore sizes around several μm can be reached. However, the use of functionalized GN/CB leads to the apparition of a homogeneous nanoporous structure, with very small pore sizes (around 0.3 μm) with high cell densities (see **Figure 5g**). As no GN/CB particles are observed, we assume that graphene could be in the cell walls of the structure, whereas carbon black particles are distributed along the width of the aramid film, but due to its low concentration (only 15% respect to the total GN/CB content), they were difficult to be found.

Regarding the surface porosity of porous aramid films, ~~reinforced with functionalized nanocharges was investigated from AFM surface images~~ AFM surface images (**Figure 6**) show isolated pores after the IL removal process. The presence of this surface porosity increases the specific surface, and then it can improve different film properties such as permeability (for nanofiltration applications) or swelling (for sensing in aqueous media). ~~This surface porosity was also observed in our previous work focused in the preparation of porous PMMA films using ionic liquids [24].~~ In these images, black regions represent the surface porosity, whereas yellow regions reveal the presence of the nanocharges in the surface of the film. In **Figure 6a**, functionalized NF are distributed along the whole surface. **Figure 6b** shows a regular pore distribution together with isolated NT (small yellow points) and agglomerated NT (big yellow regions). Finally, in **Figure 6c** porosity is clearly evidenced as well as the carbon black particles (circular-shaped around 10 μm size), and graphene nanoplatelets (small particles with sizes below 1 μm).

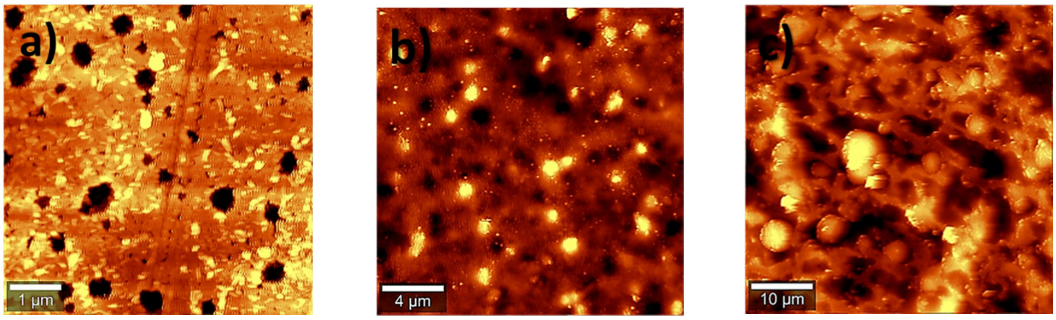

Figure 6. AFM surface profiles of porous aramid films reinforced with functionalized nanocharges. a) $(PA+NF+IL)^f$-R ; b) $(PA+NT+IL)^f$ -R ; c) $(PA+GN/CB+IL)^f$-R.

Table 2 resumes the morphological parameters of the porous aramid films, in terms of average pore radius $\bar{R}$, cell density N_c (calculated following the characterization method

of **Section 3**) and film density ρ. All the porous aramid film obtained present pore sizes below 2 μm, indicating the remarkable efficiency and simplicity of the IL removal process to obtain a regular porous structure. It is also observed that adding the nanocharges does not improve the cellular structure in terms of lower pore sizes, but reduces the film density with respect to pure porous aramid film. (F_PA+IL)-R shows a density value of 0.47 g/cm^3 and porous aramid films reinforced with nanocharges present densities between 0.29 and 0.41 g/cm^3).

However, introducing functionalized nanocharges results in a drastic reduction of the pore size, reaching radii between 240 and 470 nm, obtaining nanoporous reinforced aramids with high cell densities (≈ 10^{13}/cm^3). These films also present lower pore sizes than pure aramid films, thus reinforcing the positive effect of the functionalization process of the nanocharges in the formation of a nanoporous and homogeneous structure. It is important to remark that film density does not vary significantly in all the materials, then confirming that weight reduction depends exclusively on the proportion of IL employed in the synthesis process and not on the reinforcement.

Table 2. Morphological parameters of the porous aramid films. ($\bar{R}$ is the average pore radius, N_c the cell density and ρ is the film density taken from **Table 2**).

Film	$\bar{R}$ (μm)	N_c (1/cm^3)	ρ (g/cm^3)
(PA+IL)-R	0.52	$2.3{\cdot}10^{13}$	0.47
(PA+NF+IL)-R	1.56	$3.5{\cdot}10^{11}$	0.40
(PA+NT+IL)-R	1.91	$1.1{\cdot}10^{12}$	0.29
(PA+GN/CB+IL)-R	1.87	$2.5{\cdot}10^{11}$	0.41
(PA+NF+IL)^f-R	0.45	$3.3{\cdot}10^{13}$	0.48
(PA+NT+IL)^f-R	0.47	$3.1{\cdot}10^{13}$	0.38
(PA+GN/CB+IL)^f-R	0.24	$4.1{\cdot}10^{13}$	0.42

4.5 Thermal behavior

4.5.1 DSC curves

No great variations in the glass transition region are detected when adding the nanocharges, as observed in the DSC curves of pure and reinforced dense aramid films (**Figure S9** of the **ESI**). Pure dense aramid film PA shows a glass transition temperature of around 270 ºC and the reinforced dense aramid films ((PA+NT), (PA+GN/CB) and (PA+NF)) show glass transition values in the same range (270-275 ºC). DSC curve of the dense aramid film containing the IL ((PA+IL)), evidences the melting of the IL (around 100 ºC) and the glass transition of the aramid (around 250 ºC, lower than aramid films without IL). This behavior shows that the aramid and the IL are

phase separated, but a small plasticization effect is still present due to the glass transition reduction observed in the aramid phase (around 20 ºC respect to pure PA). **Figure S10** of the **ESI** presents the comparative DSC curves of (PA+NT), (PA+NT+IL) and (PA+NT+IL)-R, to test the thermal characteristics of films before and after the IL removal. ~~The presence of the IL is observed in the melting region around 100 ºC (red line)~~. After the IL removal process, the IL melting region at 100ºC completely disappears, then confirming the efficiency of the immersion in distilled water as a simple mechanism to eliminate the IL. Glass transition temperatures of (PA+NT), ~~black line,~~ and (PA+NT+IL)-R, ~~blue line,~~ are very similar (around 275 ºC in both cases).

4.5.2 TGA measurements

TGA curves of aramid films are presented in **Figures S11**, **S12** and **S13** of the **ESI.** Thermogravimetric data shows that pure and reinforced films (**Figure S11**) with NF and NT present a similar behavior in terms of thermal stability, as it is evidenced in the evolution of the weight loss ~~depicted in the black curve (pure aramid film) compared to red and green curves~~. On the other hand, the use of GN/CB black as reinforcing nanocharges leads to a higher thermal stability at high temperatures (above 450 ºC).

The effect of the functionalization of the nanocharges, is analyzed in **Figure S12**, in which TGA curves of reinforced aramid films with nanocharges ~~(solid lines)~~ and functionalized nanocharges ~~(dashed lines)~~ are compared**,** showing that functionalization of the nanocharges increases the thermal stability of the aramid films only at high temperatures, reducing the weight loss above 400 ºC. This effect is remarkable in the case of NF and GN/CB (**Figures S12a** and **S12b**), but it seems much lower when functionalized NT are employed (**Figure S12c**). It is also evidenced that the effect of the functionalization is less important at lower temperatures.

The IL removal process in distilled water was also analyzed through the TGA curves (**Figure S13**). It is clear that film with IL ((PA+NT+IL)) shows the weight loss associated to the IL from 300 ºC. Then, after IL removal in distilled water thermal stability of (PA+NT) and (PA+NT+IL)-R films are very similar, thus confirming the IL elimination through the immersion in distilled water.~~, which is in agreement with our previous work [19].~~

To resume the thermal behavior of aramid films, **Table 3** lists the thermal properties of dense aramid films. From the TGA experiments, onset temperature and temperatures were 5 and 10%wt. of mass loss were determined. In the case of DSC experiments, glass transition temperature was measured.

Table 3. Thermal properties of dense aramid films, measured in N_2 atmosphere. (*Onset temperature* is defined as the temperature at which the decomposition of the material begins, $T_{5\%}$ and $T_{10\%}$ are the temperatures where 5 and 10%wt. of mass loss and T_g is the glass transition temperature). *LOI* represents the "Limiting Oxygen Index", calculated from the TGA data (LOI = 17.5 + 0.4·CR, where CR is the char yield in % weight at 800 ºC under N_2 atmosphere) [27].

Film	*Onset temperature* (ºC)	$T_{5\ \%}$ (ºC)	$T_{10\ \%}$ (ºC)	T_g (ºC)	*LOI*
(PA)	438	421	459	269	40
(PA+IL)	247	225	295	251	26
(PA+NF)	441	424	457	271	41
(PA+NT)	431	439	458	273	43
(PA+GN/CB)	439	440	470	272	42
(PA+NF)[f]	445	413	460	274	45
(PA+NT)[f]	435	440	460	273	43
(PA+GN/CB)[f]	442	448	472	275	43

4.6 Mechanical properties

Tensile tests curves included in **Section S8** of the **ESI** represent the stress σ (MPa) as a function of unitary deformation ε. To compare properly the data from dense and porous films, relative values of Young's modulus and stress at break point (ratio between bulk values). We will separate the analysis in two separate groups, dense films and porous films.

a) Dense films

Figure 7 presents the effect of the addition of nanocharges in the mechanical properties of dense aramid films. It is observed that the addition of nanocharges improves slightly the mechanical behavior respect to pure PA. Especially higher values of deformation at break are detected in reinforced films, although the stress at break is only improved when NT and GN/CB are added. In the case of NF, probably due to the poor dispersion, the stress at break is reduced respect to PA, then confirming the negative influence of the poor dispersion of the nanocharge in the mechanical performance of the material.

Figure 8 shows the tensile curves obtained in dense aramid films reinforced with functionalized nanocharges. The improvement of the dispersion of the NF is evidenced in the mechanical behavior, enhancing both stress and deformation at break values. However, this effect is much more remarkable in the case of NT and GN/CB, in which the functionalization leads to a greater improvement of stress and deformation at break

values respect to pure PA film. Thus, it can be concluded that the dispersion of the nanocharges and mechanical performance are intimately related in dense aramid films.

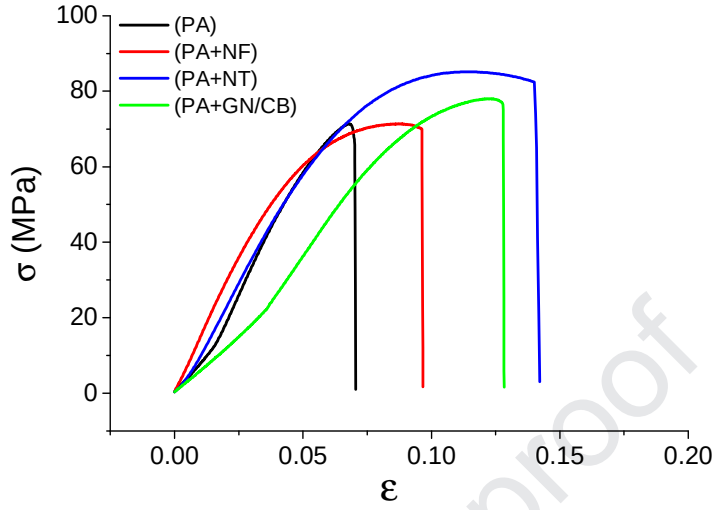

Figure 7. Tensile tests of (PA), (PA+NF), (PA+NT) and (PA+GN/CB) films.

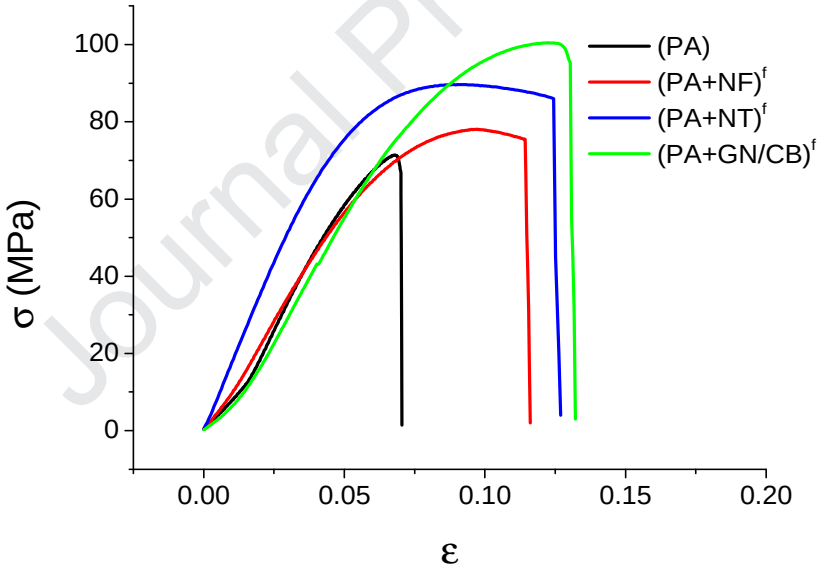

Figure 8. Tensile tests of (PA), (PA+NF)^{f}, (PA+NT)^{f} and (PA+GN/CB)^{f} films.

b) Porous films

~~The generation of the porous structure has been analyzed in the cross-section of SEM images presented in **Section 4.4**. A very regular nanoporous structure was detected in pure porous aramid films. Also, the addition of nanocharges did not improve the porous morphology of reinforced films, with pore sizes higher than the observed in porous aramid films (see **Table 1**).~~ As mentioned before, the addition of nanocharges did not

improve the porous morphology of reinforced films. This behavior is also reflected in the tensile curves presented in **Figure 9**. The tensile curve of pure porous aramid film ((PA+IL)-R) shows the highest value of stress at break. The addition of nanocharges reduces this value significantly, specially accused in the case of using neat NF, in which the stress at break reaches only a value of 11 MPa. This phenomenon is clearly related to the poor dispersion of the pure NF, ~~observed in the cross-section of the porous film (**Figure 5b**), showing the poorest porous morphology of all the films analyzed~~, revealing that the mechanical performance of porous films is intimately related to the homogeneity and pore size of the porous structure.

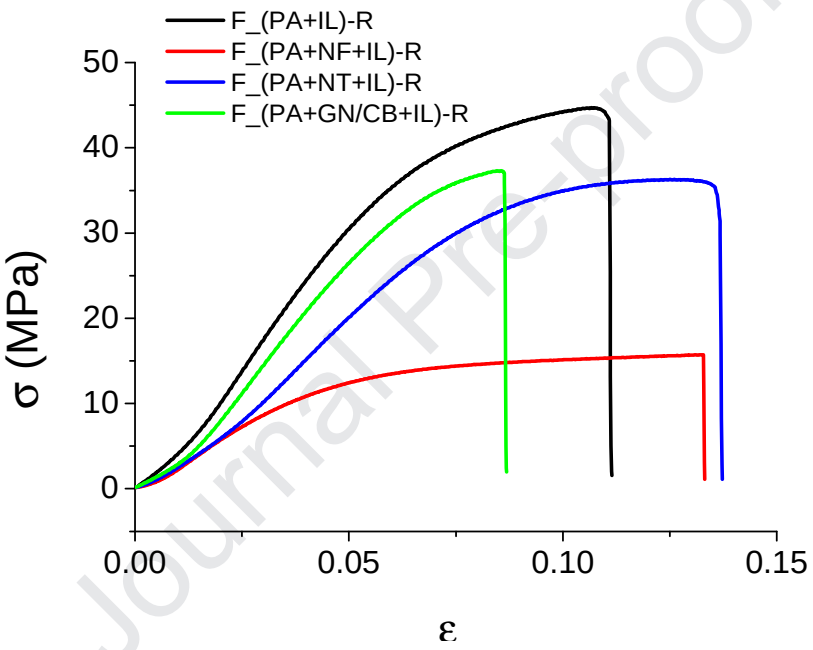

Figure 9. Tensile tests of (PA), (PA+NF+IL)-R, (PA+NT+IL)-R and (PA+GN/CB+IL)-R films.

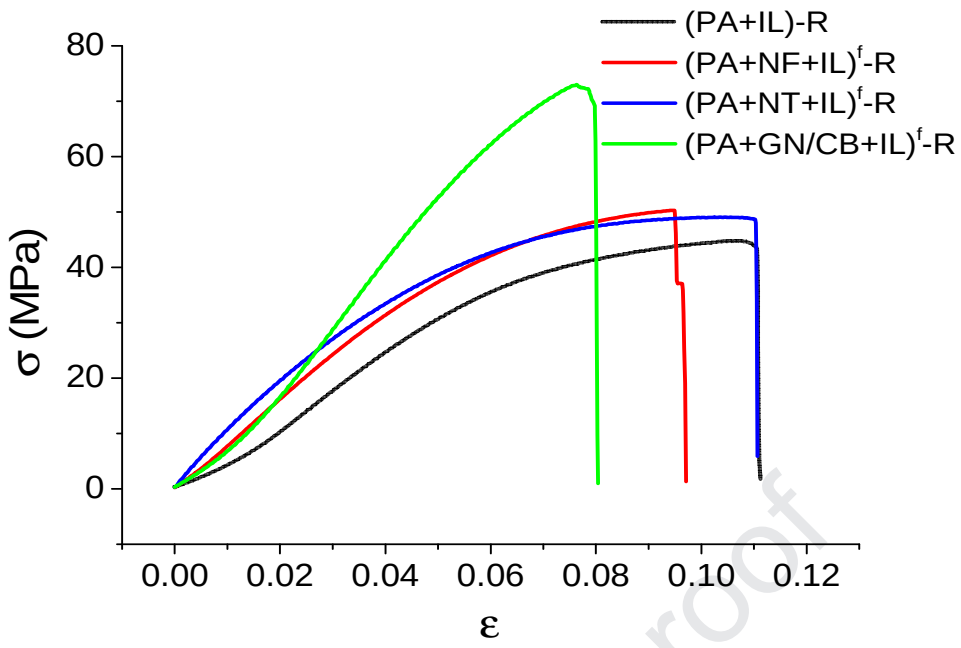

Figure 10. Tensile tests of (PA+IL)-R, (PA+NF+IL)^f-R, (PA+NT+IL)^f-R and (PA+GN/CB+IL)^f-R films.

As mentioned, the addition of functionalized nanocharges improved the morphology of the porous structure ~~in terms of pore size and cell density~~ respect to aramids reinforced with neat nanocharges. ~~(As seen in **Figures 5c, 5e and 5g**).~~ Mechanical data also reflect this behavior, as it is shown in the stress-deformation curves presented in **Figure 10**. Porous aramid films with functionalized NT show higher values of stress at break than porous films reinforced with NT. Considering the functionalization of NF, we can observe an improvement in the mechanical properties of porous films, reaching a value of stress at break point around 45 MPa, in contrast to porous aramid film reinforced with NF, which presented very low mechanical performance ($\sigma \approx 10$ MPa, as seen in **Figure 9**). **Figure 10** also shows the outstanding behavior of porous aramid films reinforced with functionalized GN/CB. In this case, the structure reaches the lowest pore sizes (around 240 nm, twice lower than pure aramid film and films reinforced with NF and NT, see **Table 2**). It seems that this reduction in the pore size implies a strong increase of the stress at break point ($\sigma \approx 70$ MPa) compared to the values obtained in the other porous films (between 40 and 45 MPa); which ~~This mechanical performance~~ is derived from the homogeneous nanoporous structure. ~~presented in **Figure 5g**~~.

The relative values of the mechanical parameters analyzed, the relative Young's modulus E_r and the relative stress at break point σ^{bp}_r. are listed in **Table S2 of the ESI**.

Four different analysis can be carried out. First, considering pure aramid films, the generation of porous structure increases significantly the relative Young's modulus respect to dense film (from 1.1 to 1.6 (GPa/(g/cm^3)), while keeping the relative stress at break point around 86 MPa/(g/cm^3). In this sense, the porosity influences positively the mechanical performance of pure aramid films.

A second analysis is focused on the addition of nanocharges to dense films. Adding NT and GN/CB to dense aramid films also increases the relative Young's modulus up to values 1.4 and 1.6 GPa/(g/cm^3), respectively. On the other hand, the addition of neat NF does not vary substantially the mechanical data respect to pure aramid film, then suggesting that the poor dispersion of neat NF observed in the SEM micrographs has a negative effect in the mechanical performance of the material. The functionalization of the nanocharges increases the relative Young's modulus respect to the values measured in aramid films reinforced with nanocharges. In this sense, E_r values are between 1.5 and 2.0 GPa/(g/cm^3). For this reason, improving the nanocharges dispersion grade leads to better mechanical properties.

The third analysis is focused on the porous aramid films reinforced with nanocharges. The reinforcement with neat nanocharges does not increase notably the mechanical behavior respect to pure porous PA film, as it is shown in the data from **Table S2** of the **ESI**. Porous films reinforced with NT and GN/CB have similar relative Young's moduli values and relative stresses at break point values. In addition, the poor dispersion grade of the pure NF affects negatively to the mechanical resistance of the porous film, with lower values of E_r and $\sigma^{bp}{}_r$.

The last analysis investigates the effect of the reinforcement with functionalized nanocharges in porous aramid films. In this case, the reinforcement with functionalized NF and NT does not improve the relative Young's modulus respect to pure porous PA film (values of E_r are around 1.6 GPa/(g/cm^3), but stress at break point $\sigma^{bp}{}_r$ is increased up to values of 94 and 113 MPa/(g/cm^3), respectively. However, the addition of functionalized GN/CB leads to the formation of a regular nanoporous structure with very low pore sizes, and relative Young's modulus and stress at break point reach values of 2.3 GPa/(g/cm^3) and 161 MPa/(g/cm^3). These values are considerably higher than the rest of the values observed in the films (porous or dense), doubling, for example, the values observed in pure dense PA films.

5. Conclusions

The present work investigates nanoporous reinforced aramids through the use of ionic liquids as porosity promoters. Reinforcements employed were carbon-based nanocharges (graphene with carbon black (GN/CB), carbon nanofibers (NF) and carbon nanotubes (NT)), and because of the low dispersion properties in the aramid matrix, a novel functionalization process is presented, anchoring a polyamide model to the nanocharge surface, improving the dispersion, thus obtaining more homogeneous reinforced aramids.

Micro and nano porosity was generated by simply immersing the samples in distilled water, obtaining controlled nanoporosity combined with high density reduction. It was detected a positive influence of the functionalization process of the nanocharges in the porous morphology, especially in the case of the functionalized GN/CB, leading to pore sizes of 250 nm. These results can be also translated to the mechanical properties of the aramid films, which were remarkably improved in the case of porous aramid films reinforced with functionalized GN/CB. Then, it is clear the direct correlation between the dispersion improvement, the obtention of finer nanoporous structures and the enhancement of mechanical properties in reinforced aramid films.

In short, these novel results confirm that reinforced porous aramid films can be easily obtained, with very low density and improved mechanical properties in respect to solid films. This investigation could open a new research field concerning these materials, in terms of using different nanocharges or functionalization processes, in order to improve the dispersion in the aramid matrix, producing high-performance nanoporous aramids suitable in many applications, such as nanofiltration, energy storage or sensing devices.

Acknowledgments

The financial support provided by FEDER (Fondo Europeo de Desarrollo Regional) and both the Spanish Agencia Estatal de Investigación (MAT2017–84501-R) and the Consejería de Educación-Junta de Castilla y León (BU306P18) is acknowledged.

Authors would also like to thank Dra. Belén Notario and Dr. David Larreina, from the CENIEH (Centro Nacional de Investigación sobre la Evolución Humana, Burgos), who were in charge of the SEM measurements, and Alberto Rodríguez Aliste, of the Parque Científico of the University of Valladolid, in charge of the TEM observations.

References

[1] J.A. Reglero Ruiz, M. Trigo-López, F. García García, J.M. García Pérez, Functional aromatic polyamides, Polymers, 9 (2017) 414. https://doi.org/10.3390/polym9090414.

[2] K. Marchildon, Polyamides-Still strong after seventy years, Macromol. React. Eng., 5 (2011) 22-54. https://doi.org/ 10.1002/mren.201000017.

[3] K. Song, Y. Zhang, J. Meng, E. C. Green, N. Tajaddod, H. Li, M. L. Minus, Structural polymer-based carbon nanotube composite fibers: Understanding the processing-structure-performance relationship, Materials, 6 (2013) 2543-2577. https://doi.org/10.3390/ma6062543.

[4] J.N. Coleman, U. Khan, W.J. Blau, Y.K. Gun'ko. Small but strong: a review of the mechanical properties of carbon nanotube polymer composites, Carbon, 44 (2006) 1624-1652. https//doi.org/10.1016/j.carbon.2006.02.038.

[5] S. Mallakpour, S, Soltanian,Surface functionalization of carbon nanotubes: fabrication and applications, RSC Adv., 6 (2016) 109916-109935. https://doi.org/10.1039/C6RA24522F.

[6] B. Dinesh, A. Bianco,C. Ménard-Moyon,Designing multimodal carbon nanotubes by covalent multi-functionalization, Nanoscale, 8 (2016) 18596-18611. https://doi.org/10.1039/C6NR06728J.

[7] V. Datsyuk, M. Kalyva, K. Papagelis, J. Parthenios, D. Tasis, A. Siokou, I. Kallitsis, C. Galiotis, Chemical oxidation of multiwalled carbon nanotubes, Carbon, 46 (2008) 833-840. https://doi.org/10.1016/j.carbon.2008.02.012.

[8] L. T. M. Hoa, Characterization of multi-walled carbon nanotubes functionalized by a mixture of HNO3/H2SO4, Diam. Relat. Mater., 89 (2018) 43-51. https://doi.org/10.1016/j.diamond.2018.08.008.

[9] I. O'Connor, H. Hayden, J.N. Coleman, Y.K. Gun'ko, High-strength, high-toughness composite fibers by swelling kevlar in nanotube suspensions, Small, 5 (2009) 466-469. https://doi.org/10.1002/smll.200801102.

[10] E.D. LaBarre, X. Calderon-Colon, M. Morris, J. Tiffany, E. Wetzel, A. Merkle, M. Trexler, Effect of a carbon nanotube coating on friction and impact performance of kevlar, J. Mater. Sci., 50 (2015) 5431-5442. https://doi.org/10.1007/s10853-015-9088-8.

[11] Y.G. Jeong, G.W. Jeon, Microstructure and performance of multiwalled carbon nanotube/*m*-aramid composite films as electric heating elements, ACS Appl. Mater. Interfaces, 5 (2013) 6527-6534. https://doi.org/10.1021/am400892k.

[12] G.W. Jeon, Y.G. Jeong, Electric heating films based on *m*-aramid containing hybrid fillers of graphene and carbon nanotube nanocomposites, J. Mater. Sci., 48 (2013) 4041-4049. https://doi.org/10.1007/s10853-013-7216-x.

[13] X. Gong, Y. Liu, Y. Wang, Z. Xie, Q. Dong, M. Dong, H. Liu, Q. Shao, N. Lu, V. Murugadoss, T. Dingh, Z. Guo, Amino graphene oxide/dopamine modified aramid fibers: Preparation, epoxy nanocomposites and property analysis, Polymer, 168 (2019) 131-137. https://doi.org/10.1016/j.polymer.2019.02.021.

[14] O. Rodríguez-Uicab, F. Avilés, P.I González-Chi, G. Canché-Escamilla, S. Duarte-Aranda, M. Yazdani-Pedram, P. Toro, F. Gamboa, M.A. Mazo, A. Nistal, J. Rubio, Deposition of carbon nanotubes onto aramid fibers using as-received and chemically modified fibers, Appl. Surf. Sci., 385 (2016) 379-390. https://doi.org/10.1016/j.apsusc.2016.05.037.

[15] J. Zhu, W. Cao, M. Yue, Y. Hou, J. Han, M. Yang, Strong and stiff aramid nanofiber/ carbon nanotube nanocomposites, ACS Nano, 9 (2015) 2489-2501. https://doi.org/10.1021/nn504927e.

[16] S.R. Kwon, J. Harris, T. Zhou, D. Loufakis, J.G. Boyd, J.L. Lutkenhaus, Mechanically strong graphene/aramid nanofiber composite electrodes for structural energy and power, ACS Nano, 11 (2017) 6682-6690. https://doi.org/10.1021/acsnano.7b00790.

[17] I. Tsivintzelis, A.G. Angelopoulou, C. Panayiotou, Foaming of polymers with supercritical CO_2: An experimental and theoretical study, Polymer 48 (2007) 5928-5939. https://doi.org/10.1016/j.polymer.2007.08.004.

[18] B.S. Pascual, M. Trigo-López, C. Ramos, T. Sanz, J.L. Pablos, F. García, J.A. Reglero, J.M. García, Microcellular foamed aromatic polyamides (aramids). Structure, thermal and mechanical properties, Eur. Polym. J. 110 (2019) 9-13. https://doi.org/10.1016/j.eurpolymj.2018.11.007.

[19] B.S. Pascual, M. Trigo-López, J.A. Reglero, J.L. Pablos, J.C. Bertolín, C. Represa, J.V. Cuevas, F. García, J.M. García, Porous aromatic polyamides the easy and green way, Eur. Polym. J. 116 (2019) 91-98. https://doi.org/10.1016/j.eurpolymj.2019.03.058.

[20] Process for the preparation of graphene, US Patent 2014/0044968 A1.

[21] L. Oliveira-Salmazo, A. López-Gil, F. Silva-Bellucci, A.E. Job, M.A. Rodríguez-Pérez, Natural rubber foams with anisotropic cellular structures: Mechanical properties and modelling, Ind. Crop. Prod., 80 (2016) 26-35. https://doi.org/10.1016/j.indcrop.2015.10.050.

[22] J.A. Reglero Ruiz, S. Vallejos, Blanca S. Pascual, C. Ramos, S. Beltrán, Félix C. García, José M. García, Microcellular polymer films based on cross-linked 1-vinyl-2-pyrrolidone and methyl methacrylate, J. Supercrit. Fluid., 140 (2018) 270-278. https://doi.org/10.1016/j.supflu.2018.07.011.

[23] M. Trigo-López, J.L. Barrio-Manso, F. Serna, F.C. García, J.M. García, Crosslinked aromatic polyamides: A further step in high-performance materials, Macromol. Chem. Phys., 214 (2013) 2223-2231. https://doi.org/10.1002/macp.201300342.

[24] M. Trigo-López, S. Vallejos, J.A. Reglero Ruiz, C. Ramos, S. Beltrán, F.C. García, J.M. García, Fabrication of microporous PMMA using ionic liquids: An improved route to classical $ScCO_2$ foaming process, Polymer, 183 (2018) 121867. https://doi.org/10.1016/j.polymer.2019.121867.

[25] S. Vallejos, J.A. Reglero, F.C. García, J.M. García, Direct visual detection and quantification of mercury in fresh fish meat using facilely prepared polymeric sensory labels, J. Mater.Chem. A, 5 (2017) 13710. https://doi.org/10.1039/c7ta03902f.

[26] J. Pinto, M. Dumon, M. Pedros, J.A. Reglero Ruiz, M.A. Rodriguez-Pérez, Nanocellular CO_2 foaming of PMMA assisted by block copolymer nanostructuration. Chem. Eng. J., 243 (2014) 428-435. https://doi.org/10.1016/j.cej.2014.01.021.

[27] D.W. van Krevelen, K. te Nijenhuis, Properties of Polymers, fourth ed., ElSevier Science, 2009.

- Nanoporous reinforced aramids have been produced using ionic liquids
- Carbon-based nanocharges were used as matrix reinforcements
- A novel functionalization process improved the dispersion of the nanocharges
- Pore sizes of 250 nm and relative Young's moduli values of 2.3 GPa·$(g{\cdot}cm^{-3})^{-1}$ were obtained

The effect of the functionalization of nanocharges is also analyzed in the comparative cross-section SEM images of porous aramid films reinforced with nanocharges. A clear inhomogeneous structure is observed for the aramid film reinforced with NF, where NF are concentrated in half of the width (**Figure 6b**) coinciding with a porous structure. However, the film presents a solid region in which no porous structure is evidenced, so a relationship between the deficient dispersion of the NF and the inhomogeneity of the porous structure can occur. ~~Considering that the porous structure is generated by the IL removal process, it seems to be a direct relation between the NF and IL dispersion in the initial DMAc solution, resulting in a very inhomogeneous structure~~. On the contrary, the functionalization of the NF leads to a very different porous structure (**Figure 6c**), thus obtaining a homogeneous porous morphology with small pore sizes and high cell densities. To conclude, both SEM images also shows isolated fibers along the porous structure~~, which are embedded in the polymer matrix, as also observed in the AFM images~~.

The effect of the functionalization in the porous aramid films reinforced with NT is also remarkable (**Figure 6d** and **e**). A microporous structure of pore size around several μm is obtained for the aramid reinforced with non-functionalized NT (**d**), very different from the morphology observed in the case of pure aramid. The addition of NT hinders the formation of a fine nanoporous structure, while using functionalized NT (**e**) reduces drastically the pore size below 1 μm, then reaching the nanoporous range, in a very fine a homogeneous structure. In this case, isolated NT were not observed, but it is possible that due to their low size they could be along the cell walls in the porous structure.

The porous structure obtained for aramids reinforced with GN/CB is very similar to the one observed for the NF (**Figure 6f**). In this case, the use of GN/CB does not improve the morphology of pure aramid film, and only pore sizes around several μm can be reached. However, the use of functionalized GN/CB leads to the apparition of a homogeneous nanoporous structure, with very small pore sizes (around 0.3 μm) with high cell densities (see **Figure 6g**). As no GN/CB particles are observed, we assume that graphene could be in the cell walls of the structure, whereas carbon black particles are distributed along the width of the aramid film, but due to its low concentration (only 15% respect to the total GN/CB content), they were difficult to be found.

Declaration of interests

☒ The authors declare that they have no known competing financial interests or personal relationships that could have appeared to influence the work reported in this paper.

☐The authors declare the following financial interests/personal relationships which may be considered as potential competing interests: